Study of Supersonic Microjet from a Square Convergent Nozzle by the Mach-Zehnder Interferometer

Tatsuya Sakanashi, Shinichiro Nakao, Yoshiaki Miyazato, and Yojiro Ishino

Abstract The three-dimensional density field of a supersonic microjet issued from a square convergent nozzle with a cross-sectional area of 1 mm × 1 mm at the exit is measured by the Mach-Zehnder interferometer with the finite fringe setting. The experiment is performed at a nozzle pressure ratio of 4.0 to produce underexpanded free jets. Interferogram analyses for reconstructing the density field of the microjet are performed using the convolution back projection (CBP) algorithm in which the analysis of the phase shift of the deformed fringe relative to the background fringe is carried out by the Fourier-transform method. A flow topology of the microjet is clarified with various visual representations.

Keywords Supersonic microjet · Square nozzle · Mach-Zehnder interferometer

1 Introduction

There has been considerable research on the subject of the dynamics of a supersonic microjet for the application of microscale devices, including a small satellite thruster in space engineering [1], a critical nozzle for obtaining mass-flow rate at a low Reynolds number [2], and a micro-propulsion nozzle [3]. A detailed comprehension of the flow characteristics through such devices requires information regarding the quantitative velocity, density, and temperature measurements in the flow field. Although, the structure of supersonic microjets was systematically studied by Scroggs & Settles [4], a detailed understanding of the flow structure of rectangular supersonic microjets is lacking in the current literature because of a challenging issue.

T. Sakanashi (✉) · S. Nakao · Y. Miyazato
The University of Kitakyushu, 1-1, Hibikino, Wakamatsu-ku, Kitakyushu 808-0135, Japan

Y. Ishino
Nagoya Institute of Technology, Gokiso-cho, Showa-ku, Nagoya 466-8555, Japan

S. N. Atluri and I. Vušanović (eds.), *Computational and Experimental Simulations in Engineering*, Mechanisms and Machine Science 98,
https://doi.org/10.1007/978-3-030-67090-0_2

For a rectangular supersonic jet operating at slightly off-design conditions, an analytical model predicting the jet flow properties has been proposed by Tam [5]. However, no exact solutions exist for a rectangular supersonic free jet with strong shock waves such as Mach shocks and intercepting shocks, or with shock wave-vortex interactions. On the other hand, as a computational fluid dynamic (CFD) analytical tool, the Reynolds averaged Navier-Stokes (RANS) simulations have been used to provide reasonably accurate results within a relatively short period of computational time [6]. The RANS models rely on additional physical approximations. Therefore, it is critical that the capabilities of these models are assessed before the numerical results are accepted. To validate a computational model, reliable experimental data sets are thus very important.

In the present study, a square convergent nozzle with an exit area of 1 mm 1 mm is used for obtaining the density field of a supersonic microjet that shows complex shock structures. To this aim, the Mach-Zehnder interferometer is utilized to investigate the three-dimensional density fields of a square supersonic microjet, which could be useful for the CFD community as the validation data against their numerical simulations of shock-containing square microjets.

2 Experimental Apparatus

The experiments were conducted in a blowdown compressed-air facility of the High-Speed Gasdynamics Laboratory at the University of Kitakyushu. A schematic diagram of the experimental apparatus with the Mach-Zehnder interferometer system is shown in Fig. 1. Ambient air is pressured by the compressor up to 1 MPa, and then stored in the high-pressure reservoir consisting of two storage tanks with a total capacity of 2 m^3 after being filtered and dried. The high-pressure dry air from the reservoir is stagnated in a plenum chamber as shown in Fig. 1, and then discharged into the atmosphere through a test nozzle. In the present experiment, the plenum pressure was controlled and maintained constant at a value of p_{os} = 407.6 kPa ± 0.5 kPa during the testing by a solenoid valve. As schematically shown in Fig. 2, a square convergent nozzle with 6 mm and 1 mm in height at the inlet and exit was used as a test nozzle. The nozzle wall contour from the inlet to exit was designed based on a sinusoidal curve so as to realize smooth uniform flows at the inlet and exit. The nozzle has a constant width of 5 mm over the entire length from the inlet to the exit. The experiment was carried out at a nozzle pressure ratio (NPR) of 4.0 within an accuracy of ±1.0% to produce an underexpanded free jet with a Mach shock. The total temperature in the plenum chamber was equal to the room temperature (T_b = 300.3 K) within an accuracy of about 0.1 centigrade during the experiment. To obtain density fields in a shock-containing microjet, the quantitative flow visualization was made using the Mach-Zehnder interferometer system with a field of view of 50 mm diameter. The Reynolds number at the nozzle exit is $Re_d = 6.06 \times 10^4$, which is calculated based on the assumption of an isentropic flow from the nozzle inlet to exit. The Mach-Zehnder interferometer is an optical

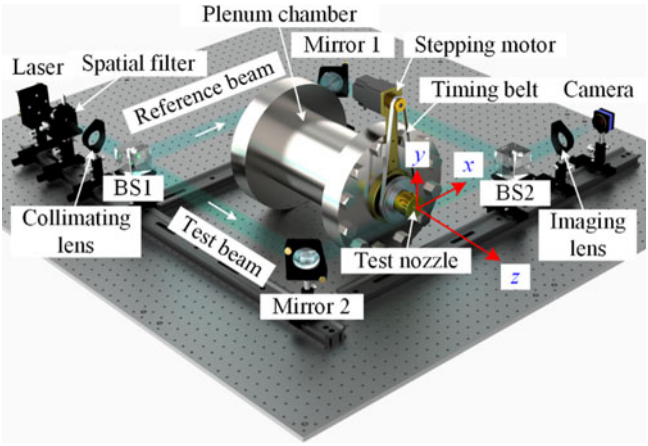

Fig. 1 Schematic drawing of experimental set up

instrument of high precision and versatility with the associated optical equipment that uses a blue semiconductor laser with a wavelength of 405 nm as a light source. The laser beam is expanded by a spatial filter to make a coherent beam before collimated into a parallel beam, and then is split into reference and test beams by a beamsplitter (BS1). The beamsplitter reflects roughly half of the intensity of the wavefront in one direction and transmits the rest in another direction. The reference beam passes through the still air and travels to another beamsplitter (BS2) after being reflected at Mirror 1. The test beam passes through a refracted index field produced by a free jet that is issued from a test nozzle and also travels to BS2 after being reflected at Mirror 2. The two beams are combined before being focused by the imaging lens and then produce interferograms on the recording medium in a digital camera.

3 Reconstruction of Jet Density Fields

3.1 Fourier Transform Method

When the test beam passes through a free jet with a variable refractive-index field, the background fringes are changed into the deformed fringe patterns because of the phase shift caused by the variations of the light speed as the beam passes through the test field. Typical profiles showing background and deformed fringe patterns are illustrated in Fig. 3. The parallel and equally spaced fringes shown as blue solid lines in Fig. 3(a) are also referred to as the wedge fringes. The interval b in Fig. 3(a) denotes the distance between two successive crests of the background fringes, and it is a function of the intersection angle between reference and test beams and the wavelength of the laser light used in the experiment. The red dashed line in Fig. 3(b)

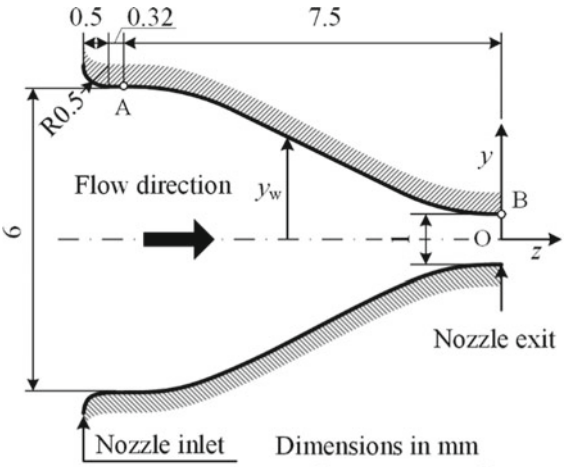

Fig. 2 Schematic of test nozzle

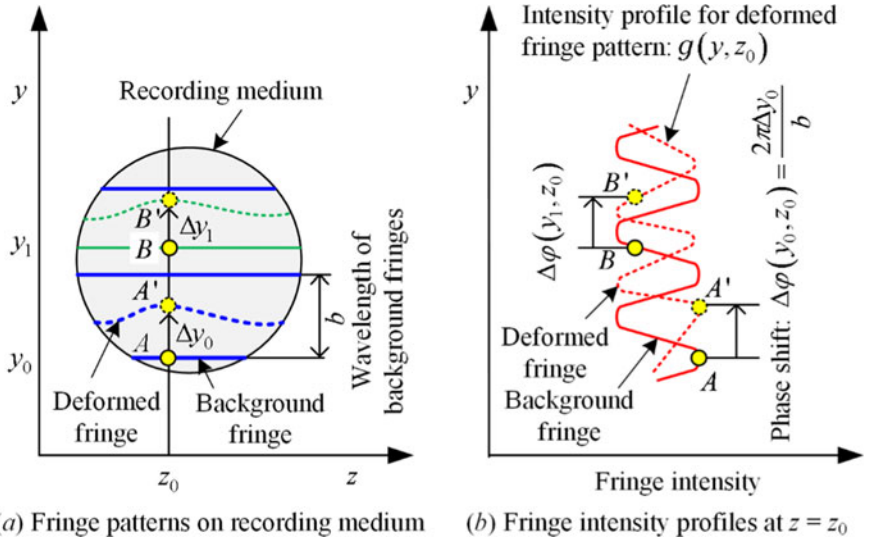

Fig. 3 Variation of background and deformed fringes by finite fringe method

shows the intensity profile $g(y, z_0)$ corresponding to the deformed fringe pattern at a particular axial position z_0, and it can be given by Takeda et al. [7], Yagi et al.[8], and Sugawara et al. [9]

$$g(y, z_0) = g_0(y, z_0) + g_1(y, z_0) \quad \cos[k_0 y - \Delta\varphi(y, z_0)] \tag{1}$$

Here, the phase shift $\Delta\varphi(y, z_0)$ contains the desired information on the density field in the free jet, and $g_0(y, z_0)$ and $g_1(y, z_0)$ represent unwanted irradiance variations arising from the nonuniform light reflection or transmission when the test beam passes through a free jet, and $k_0 = 2/b$. The coordinates y and z form the vertical plane, which is perpendicular to the test beam propagation direction, and the x-axis is taken as the direction, in which the test beam propagates after being reflected at Mirror 2 as shown in Fig. 1.

Equation (1) can be rewritten in the following expression:

$$g(y, z_0) = g_0(y, z_0) + c(y, z_0)\ \exp(ik_0 y) + c*(y, z_0)\ \exp(-ik_0 y) \tag{2}$$

With

$$c(y, z_0) = g_1(y, z_0)\ \exp\left[-i\Delta\varphi(y, z_0)\right] \tag{3}$$

where i is the imaginary unit and the asterisk * denotes the complex conjugate. The Fourier transform of Eq. (2) with respect to y is given by

$$G(k, z_0) = G_0(k, z_0) + C(k - k_0, z_0) + C*(k + k_0, z_0) \tag{4}$$

where the capital letters denote the Fourier transforms of the respective primitive functions, and k is the spatial wavenumber in the y direction. Since the spatial variations of $g_0(y, z_0)$, $g_1(y, z_0)$, and $\Delta\varphi(y, z_0)$ are slow compared with the spatial frequency k_0 when the interval between fringes is sufficiently small, the Fourier spectra in Eq. (4) are separated by the wavenumber k_0 and have the three independent peaks as schematically shown in Fig. 4(a). We make use of either of these two spectra on the carrier, say $C(k - k_0, z_0)$, and translate it by k_0 on the wavenumber axis toward the origin to obtain $C(k, z_0)$ as shown in Fig. 4(b). The unwanted background variation $G_0(k, z_0)$ has been filtered out in this stage by the pertinent bandpass filter. Applying the inverse Fourier transform of $C(k, z_0)$ with respect to the k to obtain $c(y, z_0)$ defined by Eq. (3), and taking the logarithm of Eq. (3) leads to

$$\ln\ c(y, z_0) = \ln\ g_1(y, z_0) - i\Delta\varphi(y, z_0) \tag{5}$$

Consequently, the phase shift $\Delta\varphi(y, z_0)$ in the imaginary part of (5) can be completely separated from the unwanted amplitude variation $g_1(y, z_0)$ in the real part. It is necessary to make the interval b between parallel fringes as narrow as possible to avoid islands in the fringe pattern. Wide fringes move farther away from the original location than narrower fringes, and as a result, they cover regions, which are considerably different from the optical retardations. This results in the creation of islands [10].

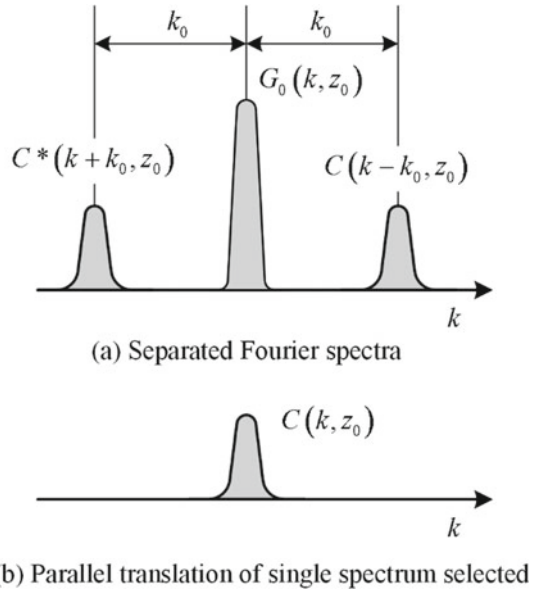

Fig. 4 Fourier-transform method for fringe-pattern analysis

3.2 Convolution Back Projection Method

Figure 5 shows a light ray travelling in the jet cross-section (x-y plane) at a fixed streamwise location $z = z_0$ of an asymmetric jet issued from a test nozzle and the phase shift from the original location of an interferogram on a recording medium where the x, y, z rectangular Cartesian coordinate system is used and the z-axis is parallel to the streamwise direction, which is also perpendicular to the x,y plane. The refractive index or density fields will now be investigated for a cross-section of z = constant. Accordingly, we omit the independent variable z in the subsequent analysis to reconstruct two-dimensional density fields.

As shown in Fig. 5, let us consider the rotated coordinates (s, t) inclined at an angle θ away from the fixed-original coordinates (x, y) where $n(x, y)$ and n_a in Fig. 5 indicate the refractive index in the jet cross-section and that of the surrounding air, respectively. Then, for a light ray traveling in the s direction with an offset of t from the axis s, the optical path difference $\Lambda_\theta(t)$ of the test beam which passed through the field with and without the jet, can be expressed by the Radon transform

$$\Lambda_\theta(t) = \int_{-\infty}^{\infty}\int_{-\infty}^{\infty} \Delta n(x, y)\delta(x\sin\theta - y\cos\theta + t)dxdy \tag{6}$$

where δ denotes the Dirac delta function and $\Delta n(x, y) \equiv n(x, y) - n_a$.

The optical path difference $\Lambda_\theta(t)$ is taken for a range of various angles from θ = 0° to 180°. The task of tomographic reconstruction in the present investigation

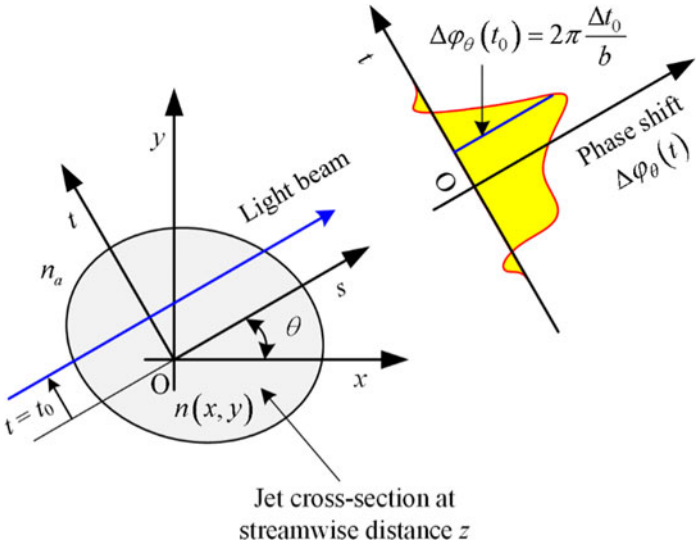

Fig. 5 Light beam passing through asymmetric refractive index field

is to find $\Delta n(x, y)$ based upon a given knowledge of $\Lambda_\theta(t)$ and then density fields can be obtained through a well-known linear relation between refractive index and density, as described later.

The transfer from the (x, y) to (s, t) coordinate systems for the integral of the right-hand side of Eq. (6) leads to

$$\Lambda_\theta(t) = \int_{-\infty}^{\infty} \Delta n(s\cos\theta - t\sin\theta, s\sin\theta + t\cos\theta)ds \tag{7}$$

After the one-dimensional Fourier transform of Eq. (7) with respect to the t variable and using the transform from the (s, t) to (x, y) coordinate systems, it reduces to a relation,

$$\begin{aligned} FT[\Lambda_\theta(t)] &\equiv \int_{-\infty}^{\infty} \Lambda_\theta(t)\exp(-2\pi it\zeta)dt \\ &= \int_{-\infty}^{\infty}\int_{-\infty}^{\infty} \Delta n(x,y)\exp[-2\pi i(ux+vy)]dxdy \end{aligned} \tag{8}$$

with $u = \zeta\sin\theta$ and $v = \zeta\cos\theta$.

Equation (8) expresses the two-dimensional Fourier transform of $\Delta n(x, y)$. Hence, the inverse Fourier transform of Eq. (8) with $u = \zeta\sin\theta$ and $\upsilon = \zeta\cos\theta$ and after some rearrangement, it reduces to

$$\Delta n(x,y) = \int_0^{\pi} \left\{ \int_{-\infty}^{\infty} |\zeta| FT[\Lambda_\theta(t)] \exp(2\pi i t\zeta) d\zeta \right\}_{t=-\sin\theta x+\cos\theta y} d\theta \tag{9}$$

The shift magnitude Δt of the deformed fringe relative to the background fringe at a fixed location ($t = const.$) on the recording medium can be given by

$$\Delta t = b\frac{\Lambda_\theta(t)}{\lambda_0} \tag{10}$$

and the phase shift $\Delta\varphi_\theta(t)$ of the deformed fringe on the recording medium can be

expressed by

$$\Delta\varphi_\theta(t) = 2\pi\frac{\Delta t}{b} \tag{11}$$

Accordingly, combination of Eqs. (9)–(11) with the Gradstone-Dale relation yields the jet two-dimensional density field at a cross-section perpendicular with respect to a fixed streamwise location z as follows:

$$\rho(x,y) = \rho_a + \frac{\lambda_0}{2\pi K}\int_0^{\pi} \left\{ \int_{-\infty}^{\infty} |\zeta| FT[\Delta\varphi_\theta(t)] \exp(2\pi i t\zeta) d\zeta \right\}_{t=-\sin\theta x+\cos\theta y} d\theta \tag{12}$$

This equation can expressed in alternative form with the convolution theorem as follows:

$$\rho(x,y) = \rho_a + \frac{\lambda_0}{2\pi K}\int_0^{\pi} [k(t) * \Delta\varphi_\theta(t)]_{t=-\sin\theta x+\cos\theta y} d\theta \tag{13}$$

where

$$k(t) \equiv FT^{-1}[|\zeta|] = \int_{-\infty}^{\infty} |\zeta| \exp(2\pi i t\zeta) d\zeta \tag{14}$$

and the symbol * denotes convolution between $k(t)$ and $\Delta\varphi_\theta(t)$.

Therefore, with the use of Eq. (13) as well as the Fourier transform method for the phase shift analysis in Sect. 3.1, the two-dimensional density fields at various streamwise locations z can be stacked together to from the three dimensional density field in a shock-containing jet. In the present study, considering the nozzle symmetry, only one-quarter between $\theta = 0$ and 45° was visualized in an equal interval of 5° to reconstruct the jet three-dimensional density field.

4 Results and Discussion

The density contour plots at the cross-section including the jet centerline are depicted in Figs. 6(a) and 6(b) where the normalized contour levels with an interval of 0.1 are shown at the top, and the spatial resolution in the experimental density map is around 4 μm. The density contour plot illustrates the various flow features of the shock cell structures quantitatively, such as the shape and size of the expansion and compression regions, the shock cell intervals, the jet boundaries, the outer shear layers near the jet boundary, and slip lines from the triple points of the Mach shock with a small Mach stem. For the jet just downstream of the nozzle exit, the jet boundary at the symmetry plane expands outwards (Fig. 6(a)), but that at the diagonal plane converges gradually toward the jet centerline (Fig. 6(b)).

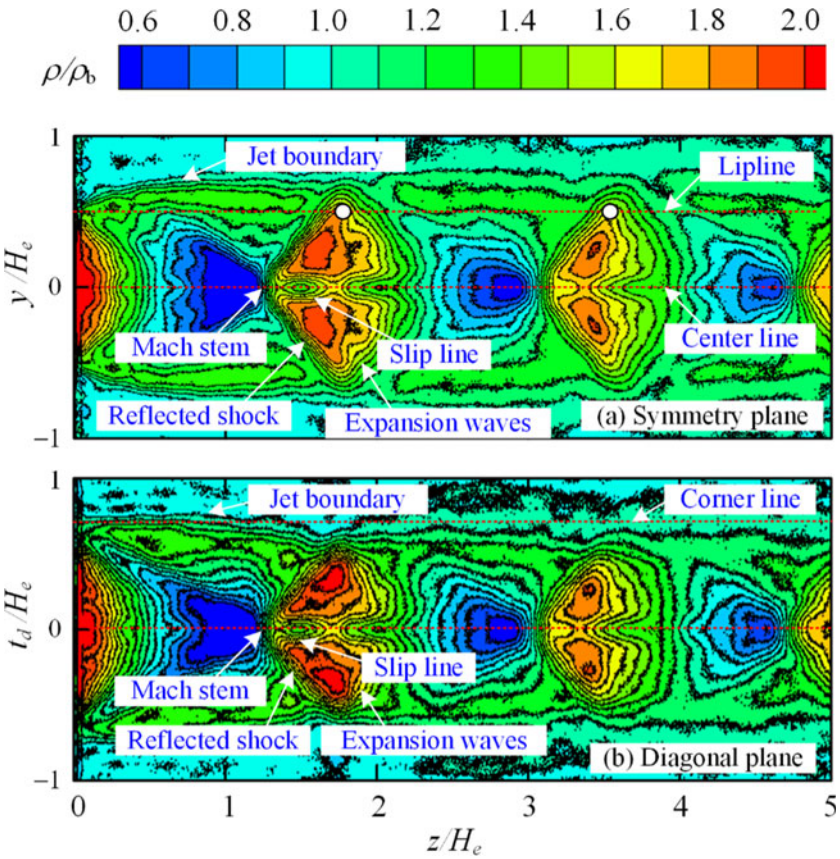

Fig. 6 Density contour plots at cross-sectional area including jet centerline

The normalized density profiles along the streamwise direction are shown in Figs. 7(a)–(c) where the theoretical density at the nozzle exit plane, which is estimated based on the assumption of the one-dimensional isentropic flow from the nozzle inlet to the exit, is shown as a leftward arrow on the vertical axis in Fig. 7(a) as a reference. The centerline density profile in Fig. 7(a) shows a representative distribution appearing in the shock-cell structure in an underexpanded free jet, i.e., the density decreases rapidly below the ambient level by expansion waves originating from the nozzle lip. This shows a sharp increase just downstream of a local minimum at z/H_e = around 1.1 and then the flow expansion and compression are repeated downstream. The local minima in the density profile gradually increase with increasing streamwise distance. Two distinct spikes (z/H_e = around 1.3 and 1.7) can be recognized just downstream of the density jump caused by the Mach stem in the first shock-cell. A similar waveform can be observed in the density

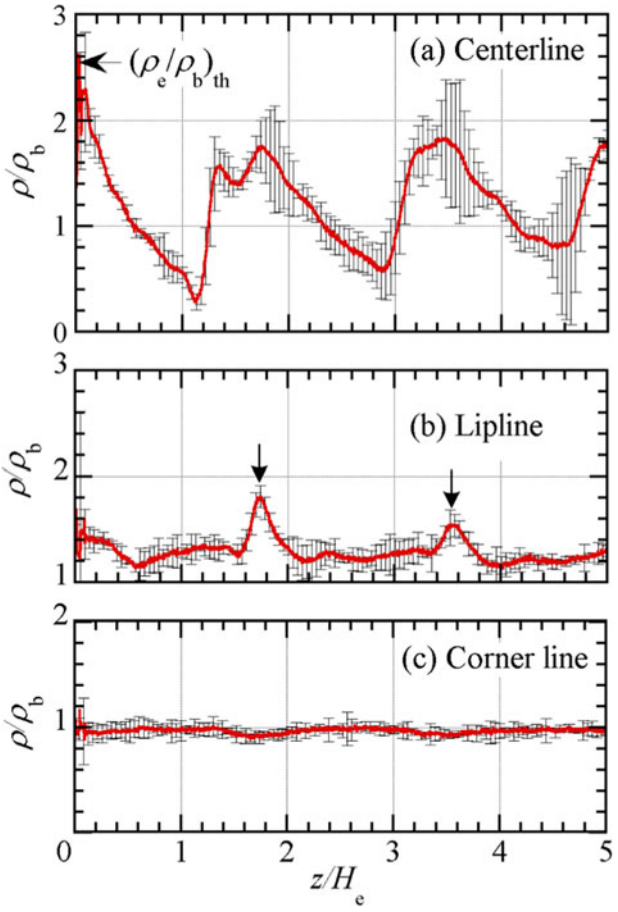

Fig. 7 Streamwise density profiles of square supersonic microjet

profile along the jet centerline obtained by the rainbow schlieren deflectometry of Takano et al. [11]. As shown with the downward arrows in Fig. 7(b), the density profile at lipline ($x/H_e = 0$, $y/H_e = 1.0$) exhibits two distinct bumps due to the reflection of the shock waves at the jet free boundary. The corresponding locations are illustrated with the open symbols in Fig. 6(a). The density profile at the corner line (Fig. 7(c)) shows almost constant variation in the streamwise direction because it is located outside the jet free boundary (see Fig. 6(b)).

5 Concluding Remarks

The Mach-Zehnder interferometer system with the finite fringe method was applied for the first time to "quantitatively" measure the density profiles over the whole density field of a square shock-containing microjet. In this experiment, a nozzle pressure ratio was constant at 4.0 to produce an underexpanded free jet with a Mach shock in the first shock cell. The microjet structures were demonstrated with the density contour plot at the cross-section including the jet centerline. It was shown that the experimental density contour plot illustrates the various flow features of the square microjet, including the shape and size of the Mach shock as well as the expansion and compression regions, the shock cell intervals, the jet boundaries, the slip streams produced from the triple points of the Mach shock and the outer shear layers near the jet boundaries. The spatial feature of the complex shock structure of the square supersonic microjet can be clearly exhibited at a high spatial resolution of 4 μm.

References

1. Lempert, W.R., Boehm, M., Jiang, N., Gimelshein, S., Levin, D.: Comparison of molecular tagging velocimetry data and direct simulation Monte Carlo simulations in supersonic micro jet flows. Exp. Fluids **34–3**, 403–411 (2003)
2. Nakao, S., Takamoto, M.: Choking phenomena of sonic nozzles at low Reynolds numbers. Flow Meas. Instrum. **11–4**, 285–291 (2000)
3. Louisos, W.F., Hitt, D.L.: Heat transfer & viscous effects in 2D & 3D supersonic micro-nozzle flows. AIAA Paper, No. 2007-3987 (2007)
4. Scroggs, S.D., Settles, G.S.: An experimental study of supersonic microjets. Exp. Fluids **21**, 401–409 (1996)
5. Tam, C.K.W.: The shock-cell structures and screech tone frequencies of rectangular and non-axisymmetric supersonic jets. J. Sound Vibr. **121–1**, 135–147 (1988)
6. Franquet, E., Perrier, V., Gibout, S., Bruel, P.: Free underexpanded jets in a quiescent medium: a review. Prog. Aerosp. Sci. **77**, 25–53 (2015)

7. Takeda, M., Ina, H., Kobayashi, S.: Fourier-transform method of fringe-pattern analysis for computer-based topography and interferometry. J. Opt. Soc. Am. **72–1**, 156–160 (1982)
8. Yagi, S., Inoue, S., Nakao, S., Ono, D., Miyazato, Y.: Optical measurements of shock waves in critical nozzles at low Reynolds numbers. J. Flow Control Meas. Visual. **5–2**, 36–50 (2017)
9. Sugawara, S., Nakao, S., Miyazato, Y., Ishino, Y., Miki, K.: Three-dimensional reconstruction of a microjet with a Mach disk by Mach-Zehnder interferometers. J. Fluid Mech. **893**, A25 (2020)
10. Winckler, J.: The Mach interferometer applied to studying an axially symmetric supersonic air jet. Rev. Sci. Instrum. **19–5**, 307–322 (1948)
11. Takano, H., Kamikihara, D., Ono, D., Nakao, S., Yamamoto, H., Miyazato, Y.: Three-dimensional rainbow schlieren measurements in underexpanded sonic jets from axisymmetric convergent nozzles. J. Thermal Sci. **25–1**, 78–83 (2016)